



Lithium niobate nanoparticles as biofunctional interface material for inner ear devices F

Cite as: Biointerphases **15**, 031004 (2020); <https://doi.org/10.1116/6.0000067>

Submitted: 04 February 2020 . Accepted: 20 April 2020 . Published Online: 20 May 2020

Serena Danti , Bahareh Azimi, Mariarita Candito, Alessandra Fusco, Mohammad Sajad Sorayani Bafqi, Claudio Ricci, Mario Milazzo , Caterina Cristallini, Masud Latifi, Giovanna Donnarumma, Luca Bruschini, Andrea Lazzeri, Laura Astolfi, and Stefano Berrettini

COLLECTIONS

Note: This paper is part of the Conference Collection on ISSIB 2019: Surface and Interface for Biomaterials.

F This paper was selected as Featured



View Online



Export Citation



CrossMark



AVS Quantum Science

Co-Published by



RECEIVE THE LATEST UPDATES

Lithium niobate nanoparticles as biofunctional interface material for inner ear devices



Cite as: *Biointerphases* 15, 031004 (2020); doi: 10.1116/6.0000067

Submitted: 4 February 2020 · Accepted: 20 April 2020 ·

Published Online: 20 May 2020



Serena Danti,^{1,2,a)} Bahareh Azimi,^{1,2,3} Mariarita Candito,⁴ Alessandra Fusco,⁵ Mohammad Sajad Sorayani Bafqi,⁶ Claudio Ricci,³ Mario Milazzo,² Caterina Cristallini,⁷ Masud Latifi,⁶ Giovanna Donnarumma,⁵ Luca Bruschini,⁸ Andrea Lazzeri,¹ Laura Astolfi,⁴ and Stefano Berrettini⁸

AFFILIATIONS

¹Department of Civil and Industrial Engineering, University of Pisa, Largo Lucio Lazzarino, 56126 Pisa, Italy

²Department of Civil and Environmental Engineering, Massachusetts Institute of Technology (MIT), Massachusetts Ave. 77, Cambridge, Massachusetts 02139, USA

³National Interuniversity Consortium of Materials Science and Technology (INSTM), via G. Giusti 9, 50121 Firenze, Italy

⁴Bioacoustics Research Laboratory, Department of Neurosciences, University of Padua, via G. Orus, 2b, 35129 Padua, Italy

⁵Department of Experimental Medicine, University of Campania "Luigi Vanvitelli," via Santa Maria di Costantinopoli 16, 80138 Naples, Italy

⁶Department of Textile Engineering, Amirkabir University of Technology (Tehran Polytechnic), Tehran 15875–4413, Iran

⁷Institutes for Chemical-Physical Processes, National Research Council (CNR-IPCF), via Moruzzi 1, 56126 Pisa, Italy

⁸Department of Surgical, Medical, Molecular Pathology and Emergency Medicine, University of Pisa, Largo Lucio Lazzarino, 56126 Pisa, Italy

Note: This paper is part of the Conference Collection on ISSIB 2019: Surface and Interface for Biomaterials.

a) Author to whom correspondence should be addressed: serena.danti@unipi.it

ABSTRACT

Sensorineural hearing loss (SNHL) affects the inner ear compartment and can be caused by different factors. Usually, the lack, death, or malfunction of sensory cells deputed to transduction of mechanic-into-electric signals leads to SNHL. To date, the therapeutic option for patients impaired by severe or profound SNHL is the cochlear implant (CI), a high-tech electronic device replacing the entire cochlear function. Piezoelectric materials have catalyzed attention to stimulate the auditory neurons by simply mimicking the function of the cochlear sensory epithelium. In this study, the authors investigated lithium niobate (LiNbO₃) as a potential candidate material for next generation CIs. LiNbO₃ nanoparticles resulted otocompatible with inner ear cells *in vitro*, had a pronounced immunomodulatory activity, enhanced human beta-defensin in epithelial cells, and showed direct antibacterial activity against *P. aeruginosa*. Moreover, LiNbO₃ nanoparticles were incorporated into poly(vinylidene fluoride-trifluoro ethylene) fibers via electrospinning, which enhanced the piezoelectric response. Finally, the resulting fibrous composite structures support human neural-like cell growth *in vitro*, thus showing promising features to be used in new inner ear devices.

Published under license by AVS. <https://doi.org/10.1116/6.0000067>

I. INTRODUCTION

Deafness is the most common sensory impairment and about 466 million people worldwide are estimated to suffer from disabling hearing loss, namely, higher than 40 dB.^{1,2} Specifically, sensorineural hearing loss (SNHL) affects the inner ear compartment and can be caused by genetic factors, noise exposure, aging, infections, and use of ototoxic drugs. Recovery from SNHL is very difficult because of the

anatomical features of the cochlea and the inability to regenerate inner ear cells and neurons that have altered or lost their function.^{2,3}

The accepted therapeutic treatments for SNHL are the intratympanic or systemic administration of steroids to attenuate the inflammation and aminoglycoside to heal infections;⁴ on the other hand, engineered devices dealing with the symptoms are available, which partially restore the hearing function without the need for damaged cell regeneration.⁵ New therapeutic approaches involve

research in pharmacological compounds, biomaterials, and nanotechnologies to obtain sensory hair cell regeneration or to prevent their damage and/or loss.^{6,7}

To date, the therapeutic option for patients impaired by severe or profound SNHL is the cochlear implant (CI), a high-tech electronic device replacing the entire cochlear function, whose implantation involves an invasive and complex surgery of the temporal bone.⁸

Drawbacks of CIs include loss of hearing frequencies, hearing sounds differently, noise, decrease of residual hearing, incomplete language understanding, problems with music perception, interactions of the implant with static electricity, magnetic fields, mobile phones, metal detectors and hearing aids, battery charge dependency, aesthetic problems and water unsuitability, and lifelong restrictions with magnetic resonance imaging (MRI).

Piezoelectric materials have recently received scientific attention in different fields, such as biomedicine and energy harvesting.^{9–11} The application of piezoelectric materials to develop novel CIs was suggested by Mukherjee *et al.*^{12,13} Piezoelectric materials' layering on the basilar membrane (BM) of the cochlea can stimulate the auditory neurons, thus mimicking the cochlear sensory epithelium.¹⁴ Unlike conventional CIs, piezoelectric CIs are biomaterial-based devices, self-powered, waterproof, and nonferromagnetic, and exploit the cochlear constitutive mechanical tonotopy (i.e., frequency selectivity along the main axis of the basilar membrane), enabling a fine-tuning process of sound vibrations.¹⁵ Polymeric materials are suitable candidates for the fabrication of cochlear microdevices, which are required to be flexible to accommodate the surgical insertion within the curvy inner ear anatomy. Moreover, polymers usually possess good processability and some of them own desirable piezoelectric properties.¹⁶ Among the piezoelectric polymers, polyvinylidene fluoride (PVDF) and its copolymers, such as poly(vinylidene fluoride-co-trifluoro ethylene) [P(VDF-TrFE)] and poly(vinylidene fluoride-co-hexafluoro propylene) [P(VDF-HFP)], show a high piezoelectric effect. The development of PVDF-based electrospun fibers for cochlear stimulation has demonstrated potential for changing the future way of treating SNHL; however, sufficient sensitivity could not be obtained so far by using plain polymers.¹³

On the other hand, piezoelectric ceramics have higher piezoelectricity than polymers, but they are rigid and difficult to process. Among them, lithium niobate (LiNbO₃) shows excellent piezoelectric properties and has recently been applied in biological engineering.^{17–20}

Different types of nanoparticles are under examination in several studies focusing on the drug delivery system in the inner ear.^{21,22} Ceramic nanoparticles have also been used in many research fields to improve regeneration and promote healing of several tissues.^{23,24} Additionally, LiNbO₃ nanoparticles have shown the ability to promote adhesion, proliferation, and migration of cells, including osteoblasts and fibroblasts.^{18,25} Thus, in perspective, they could also be used in ear pathology, for example, to repair eardrum perforations by promoting the migration of tympanic membrane fibroblasts and epithelial cells. Moreover, by virtue of their piezoelectric properties, LiNbO₃ nanoparticles could play a role in the replacement of damaged hair cells.

The first aim of this study was an extensive biological characterization of LiNbO₃ nanoparticles to be applied in the inner ear, which is a delicate organ. Indeed, acoustic sensory cells are naturally present in a limited number, with poor or no self-renewal capacity.⁵ In our

study, LiNbO₃ nanoparticles were tested with the organ of Corti cells and neural cells to assess ototoxicity and with epithelial cells to reveal immunomodulation and innate antibacterial response. Moreover, LiNbO₃ nanoparticles were tested toward ear infective bacteria to investigate direct antimicrobial effects. LiNbO₃ nanoparticles were then used for the production of piezoelectric composite P(VDF-TrFE)/LiNbO₃ fiber meshes via electrospinning. The final objective of this research was to obtain otocompatible and biofunctional nanostructured materials with improved piezoelectric properties provided with respect to those of plain P(VDF-TrFE) and morphological nano-/microfeatures attractive for neural cells, as promising piezoelectric substrates for next generation CIs.

The development of a high-performance piezoelectric biomaterial, to be used as a cochlear transducer, would improve the quality of life of deaf people since it would offer a cost-effective, simple, biomimetic, water, and magnetocompatible treatment option.

II. EXPERIMENT

A. Materials

P(VDF-TrFE) powder (70:30, mol.%) was purchased from PIEZOTECH ARKEMA (Pierre-Benite, France) and methyl ethyl ketone (MEK; code 109708) was obtained from Merck (Darmstadt, Germany). Lithium niobate powder (LiNbO₃; code 254290), gelatin (75 Bloom, type B from bovine skin), nerve growth factor (NGF), Phenazine methosulfate (PMS), 4',6-diamidino-2-phenylindole (DAPI), F12, and Roswell Park Memorial Institute (RPMI) culture media, MgCl₂, and Phalloidin Tric were purchased from Sigma Aldrich (Milan, Italy). Dulbecco's modified essential medium (D-MEM), fetal bovine serum (FBS), horse serum (HS), L-glutamine, and penicillin/streptomycin were supplied by Gibco BRL (Gaithersburg, MD, USA). Interferon γ was obtained from Genzyme (Cambridge, MA, USA). CellTiter 96[®] Aqueous MTS Reagent Powder was supplied by Promega Corporation (Madison, WI, USA). Diflucan was bought from Pfizer-Italia (Latina, Italy). SHSY-5Y cells (CRL-2266), HaCaT cells, and Eagle's minimum essential medium (E-MEM) were bought from ATCC-LGC Standards (Milan, Italy). Absolute ethanol, Gliofixx, and glycerol were supplied by BioOptica (Milan, Italy). SYBR Green kit was obtained from Roche (Basel, Switzerland) and alamarBlue from ThermoFisher Scientific (Waltham, MA, USA). Mouse Organ of Corti (OC-k3) cells were provided by House Ear Institute (Los Angeles, CA, USA).

B. Methods

1. Preparation of LiNbO₃ nanoparticle suspensions

For size distribution characterization, LiNbO₃ powder was suspended in milli-Q water and sonicated using a sonicator probe Sonics vibro cell VC130 (Sonics & Materials Inc., Newtown, CT, USA; Cycle: 0.5, Amplitude: 40, Full power 130 W) for 10 min and at 20 kHz. For cell culture experiments, sterile dispersions were needed. Therefore, sterile filtered 2% w/v gelatin or poly-L-lysine aqueous solutions were added with LiNbO₃ powder, previously UV-irradiated overnight, placed inside sterile tubes, and sonicated for 24 h via an ultrasonic bath (Bransonic sonicator 2510, Marshall Scientific, Hampton, NH, USA), using an output power of 20 W.

2. Fabrication of P(VDF-TrFE)/LiNbO₃ fibers

A P(VDF-TrFE) solution (20% w/v) was prepared through dissolution of the polymer in MEK at room temperature (RT) under mechanical stirring for about 12 h. The polymeric solution was loaded into a 10 ml glass syringe, fitted with a blunt tip stainless steel needle (21G × 3/4"), and placed into a syringe pump (NE-300, New Era Pump Systems, Inc., NY, USA). The ground terminal of high voltage supply (S1600079 Linari High Voltage, Linari Engineering s.r.l., Pisa, Italy) was connected to the metal needle, while the positive terminal was connected to the collector; 35 kV voltage was applied. A cylindrical collector (diameter = 8 cm; Linari Engineering s.r.l.) was placed at a distance of 15 cm from the tip of the needle. The polymer solution was injected from a needle in the presence of an electric field at a constant flow rate of 0.016 ml/min. The production of random-to-aligned electrospun fiber meshes was performed by collecting the polymeric jet onto the rotating collector with collector velocities of 500 and 4000 rpm. All the fabrication steps were performed at RT with relative humidity (RH) of about 46%. The fiber meshes were kept in oven at 60 °C overnight to remove traces of the organic solvent from the fibers.

The same procedure was used to produce LiNbO₃/P(VDF-TrFE) composite fibers. For the preparation of solution, first, the LiNbO₃ powder was dispersed in MEK. The suspension was sonicated (Sonics vibro cell VC130, Sonics & Materials Inc., Newtown, CT, USA) for 10 min (Cycle: 0.5, Amplitude: 40, Full power 130 W) and at a frequency of 20 kHz. Subsequently, P(VDF-TrFE) was added, and the solution (20 w/v%) was left at RT for about 12 h under mechanical stirring to form homogeneous dispersion prior to being loaded into the syringe for electrospinning, as described above. The used concentrations of the LiNbO₃ were 0%, 10%, and 20% (w/w%) with respect to P(VDF-TrFE).

3. Morphological characterization of LiNbO₃ nanoparticles and LiNbO₃ nanoparticle-incorporated fibers

The morphology of the plain nanoparticles and fiber meshes incorporating nanoceramics was evaluated by scanning electron microscopy (SEM) using a FEI FEG-Quanta 450 instrument (Field Electron and Ion Company, Hillsboro, Oregon, USA). The samples were sputter-coated with Gold (Gold Edwards SP150B, England) before analysis. SEM micrographs were acquired at different magnifications to visualize the details of interest. Image-J software (version 1.46 r; <http://imagej.nih.gov>) was used to determine the average diameter of 100 fibers from SEM images.

Energy-dispersive x-ray spectroscopy FEI FEG-Quanta 450 instrument (Field Electron and Ion Company) was used for elemental analysis of the samples. Particle size and size distribution were analyzed using a water-diluted suspension followed by bath sonication LBS2 (Falc Instruments, Treviglio, BG, Italy) in a Zetasizer Nano S90 (Malvern Panalytical, Malvern, UK).

4. Cytocompatibility of LiNbO₃ nanoparticles

All the experiments were performed on two different cell lines: OC-k3, an inner ear cell line derived from the Immortomouse® Organ of Corti widely used for ototoxicity tests, and PC12, derived

from rat pheochromocytoma, an adrenal medullary tumor, that can be differentiated into "neuronlike cells" if stimulated with the NGF.

OC-k3 cells were cultured at 33 °C and 10% CO₂ in complete culture medium, consisting of D-MEM, 10% FBS, 2 mM of L-glutamine, and 50 IU/ml of INF. PC12 cells were cultured at 37 °C and 5% CO₂ in complete culture medium, consisting of RPMI, 10% HS, 5% FBS, 2 mM of L-glutamine, and 1% penicillin/streptomycin. These cells were differentiated for 6 days by differentiating medium, which consisted of adding the growth factor NGF at 50 ng/ml into the complete culture medium. On the sixth day, once the peak of differentiation was reached, LiNbO₃ nanoparticles (200–600 nm size range) under examination were added at concentrations in the range of 0–74 ng/ml. Cytotoxicity was analyzed after 24, 48, and 72 h.

a. Vitality test with MTS assay. The cytotoxicity of nanoparticles was investigated using the MTS assay, a colorimetric method that allows the quantification of cell proliferation. The OC-k3 cells were seeded in 96-well plates at the concentration of 7000 cells/well in 100 μl of medium and left to adhere for 24 h at RT, after which were treated with the compound resuspended in a complete medium at three different concentrations: 0.85, 15, and 74 ng/ml. The PC12 cells were seeded in 6-well plates at the concentration of 5000 cells/well in 2 ml of differentiation medium and left to differentiate for 6 days and then were treated with LiNbO₃ resuspended in the differentiation medium at three different concentrations: 0.85, 15, and 74 ng/ml. Vitality was analyzed after 24, 48, and 72 h after treatment. For each timepoint, samples of untreated cells were used as a control. Each sample was tested in triplicate, and each test was repeated at least three times. At the end of each timepoint, the medium was changed with 100 μl of complete medium plus 20 μl of a mixture consisting of MTS and PMS in a ratio of 20:1 (v/v). After 3 h incubation at 37 °C, absorbance was read at 492 nm with a plate reader (SIRIO, SEAC s.r.l., Florence, Italy). The absorbance value obtained for each sample, expressed as optical density (OD = optical density), was normalized to the average OD value of the respective untreated vitality considered 100%.

b. Morphological analysis with phalloidin/DAPI staining. The morphological test was also conducted to assess the conditions of the cytoskeleton and nuclei. OC-k3 or PC12 cells were seeded on a round glass slide in each well of 6-well plates and cultured and treated as described in the previous paragraph. The sample of untreated cells to be used as a control was also produced for each time. Each sample was tested in triplicate, and each test was repeated at least two times. At the end of each time, the cells were fixed in Gliofixx for 30 min, washed three times in PBS 1×, and stained with 1 μg/ml of Phalloidin Tritic for 2 h in the dark to highlight the cytoskeleton. After two washes in 1× PBS, the cells were stained with 2 μg/ml of DAPI for 10 min in the dark to highlight the nuclei. After two washing steps in 1× PBS, the slides were mounted with 20% glycerol on an object-holder slide and finally observed under a fluorescence optical microscope Nikon Eclipse TE2000-U (Nikon, Tokyo, Japan). The images were acquired with the NIS element program (Nikon).

c. Immunomodulatory effects. Human keratinocytes HaCaT cells were grown in the D-MEM medium in the presence of 10%

TABLE I. RT-PCR details, including gene, primer sequences, operational conditions, and product size.

Gene	Primers sequence	Conditions	Product size (bp)
IL-6	5'-ATGAACTCCTTCTCCACAAGCGC-3' 5'-GAAGAGCCCTCAGGCTGGACTG-3'	5 s at 95 °C, 13 s at 56 °C, 25 s at 72 °C for 40 cycles	628
IL-8	5'-ATGACTTCCAAGCTGGCCGTG-3' 5'-TGAATTCTCAGCCCTCTTCAAAAACTTCTC-3'	5 s at 94 °C, 6 s at 55 °C, 12 s at 72 °C for 40 cycles	297
IL-1 α	5'-CATGTCAAATTTCACTGCTTCATCC-3' 5'-GTCTCTGAATCAGAAATCCTTCTATC-3'	5 s at 95 °C, 8 s at 55 °C, 17 s at 72 °C for 45 cycles	421
IL-1 β	5'-GCATCCAGCTACGAATCTCC-3' 5'-CCACATTCAGCACAGGACTC-3'	5 s at 95 °C, 14 s at 58 °C, 28 s at 72 °C for 40 cycles	708
TNF- α	5'-CAGAGGGAAGAGTTCCCCAG-3' 5'-CCTTGGTCTGGTAGGAGACG-3'	5 s at 95 °C, 6 s at 57 °C, 13 s at 72 °C for 40 cycles	324
TGF- β	5'-CCGACTACTACGCAAGGAGGTCAC-3' 5'-AGGCCGGTTCATGCCATGAATGGTG-3'	5 s at 94 °C, 9 s at 60 °C, 18 s at 72 °C for 40 cycles	439
HBD-2	5'-GGATCCATGGGTATAGGCGATCCTGTTA-3' 5'-AAGCTTCTCTGATGAGGGAGCCCTTCT-3'	5 s at 94 °C, 6 s at 63 °C, 10 s at 72 °C for 50 cycles	198

FBS, 1% Penstrep, and 1% glutamine at 37 °C in a 5% CO₂ modified atmosphere. Subsequently, they were seeded in 6-well plates until 80% of confluence and treated with LiNbO₃ at following concentrations: 5, 10, 20, 50, and 100 μ g/ml.

The treatments, repeated in triplicate, were carried out for 6 and 24 h; at these timepoints, the total RNA was isolated and 1 μ g was reverse-transcribed into complementary DNA (cDNA) using random hexamer primers, at 42 °C for 45 min, according to the manufacturer's instructions. Real time PCR for quantification of expression levels of proinflammatory cytokines: interleukin (IL)-1 α , IL-1 β , IL-6, IL-8, and tumor necrosis factor (TNF)- α , anti-inflammatory cytokine transforming growth factor (TGF)- β , and antimicrobial peptide human beta-defensin (HBD)-2 were evaluated with the LC Fast Start DNA Master SYBR Green kit using 2 μ l of cDNA, corresponding to 10 ng of total RNA in a 20 μ l final volume, 3mM MgCl₂, and 0.5 μ M sense primer and antisense primer (Table I).

d. Antibacterial activity assay. The LiNbO₃ powder was resuspended at the concentration of 1 mg/ml in a poly-L-lysine/PBS solution at 1 mg/ml and thereafter sonicated for 12 h at 20 W to obtain a stable suspension as described in Methods (Sec. I). Strains of *S. aureus* and *P. aeruginosa* were seeded on Mannitol Salt Agar and Brain Heart Infusion Agar plates, respectively. On the surface of the plates, pads of absorbent paper of 6.5 mm diameter were applied, soaked with 10 μ l of LiNbO₃ suspension (fully absorbed) at the following concentrations: 1000, 100, 50, and 25 μ g/ml.

5. Mechanical properties of P(VDF-TrFE)/LiNbO₃ fibers

The mechanical properties of scaffolds were characterized by a mechanical tester INSTRON 5500R equipped with MERLIN software (INSTRON, Massachusetts, USA). The load cell had a maximum capacity of 100 N, the crosshead speed was 5 mm/min, and the gauge length (2 cm) of the electrospun fiber meshes was determined by the gap between the parallel strips of the frame. An approximate cross section area of each mesh was measured using a thickness gauge. The dynamic mechanical analysis (DMA) was

carried out on a Gabo Eplexor® 100 N (Gabo Qualimeter®; Testanlagen GmbH, Ahlden, Germany). The strip (~2 \times 1 cm²) was cut from the fiber mesh. A constant static stress and 1% dynamic strain were applied in the tensile mode. The tests were performed in the frequency range of 5–100 Hz.

6. Crystalline and piezoelectric properties of LiNbO₃ and P(VDF-TrFE)/LiNbO₃ fibers

As the crystalline β -phase is entitled for the piezoelectric behavior,⁹ XRD and FTIR analyses were performed to assess its presence and content in the plain and composite materials. XRD patterns were also recorded on LiNbO₃ nanoparticles (Siemens D 500 Krystalloflex 810, Munich, Germany) using Cu K α radiation (λ = 1.5406 Å) in the reflection mode at a scanning rate of 0.03°/s with 2 θ in the range of 20°–80° and a temperature of 25 °C. Differential scanning calorimetry (DSC; TA Q200, New Castle, USA) was used to determine the melting temperature (T_m) and crystalline content of electrospun fiber meshes. DSC experiments were performed by applying a heat-cool-heat temperature variation in the range from -70 °C to +250 °C with a heating rate of 10 °C/min and a cooling rate of 5 °C/min, respectively. The crystallinity of samples was then calculated using the following equation:

$$X_c(\%) = \frac{H_{fs}}{H_{ft}} \times 100, \quad (1)$$

where H_{fs} is the measured heat of fusion to obtain the melting of the sample and H_{ft} is the heat of fusion for 100% crystalline P(VDF-TrFE) (91.45 J/g).²⁶

The FTIR spectra of the fiber samples were recorded with a Perkin Elmer Spectrum GX spectrometer using a polarized wire grid (Perkin Elmer, Massachusetts, USA). The beam, directed orthogonally to the wider specimen surface, was polarized alternatively parallel or orthogonal to the main axis of the fiber. In the case of anisotropic meshes as obtained using the rotating collector, this measurement allows the evaluation of the influence of collector velocity on the P

(VDF-TrFE) crystalline phase content of the samples. All the spectra were collected in the mid-IR region ($500\text{--}1500\text{ cm}^{-1}$) using 16 scans.

A self-designed mechanical-electronic evaluation system (PiezoTester) was also used to measure the output voltages of the samples (Fig. 1).²⁷ With this method, after applying a predetermined load to the samples, their electrical output is measured by an oscilloscope. The system has also the ability to evaluate the piezoelectric properties of devices with different loading frequencies. In this case, the load was applied to the specimen by means of a step motor, a radial movement adjustable disc cam (that converts rotation movement to a vertical displacement), follower (a shaft with vertical movement), and an impact head with various cross section shapes to change the effective surface. Finally, an electrical shield was used to protect samples from electrical ambient noises. Effectively applied forces were measured by a load cell located exactly below the sample. The final output was observed using a digital oscilloscope with high internal impedance to record and present the data in analog or digital forms. One of the main positive points of this measuring approach is the possibility to measure the applied pressure, which makes it possible to evaluate the sensitivity value of devices (defined as output voltage/applied load) with predefined forces and frequencies. In order to fabricate a sample for PiezoTester, a nanofiber mesh of $0.5 \times 1.0\text{ cm}^2$ size was used as an active layer between two aluminum foils as collectors. To reduce the effect of thickness on the output voltage, the sensitivity of the layers was normalized by the thickness, measured by an SDL34 Shirley fabric thickness tester (based on hydrophilic ASTM D1777).

7. Cytocompatibility of P(VDF-TrFE)/LiNbO₃ fibers

P(VDF-TrFE)/LiNbO₃ fibers at concentration 0%, 10%, and 20% (w/w%) were cultured for 7 days with SHSY-5Y cells ($n = 3$). SHSY-5Y is a human neuroblastoma-derived cell line known to be dopamine β -hydroxylase active and express neural markers, thus representing a valuable model of human neural cells for *in vitro* tests. Cryopreserved cells were defrosted and expanded in the growth medium composed of 1:1 (v/v) E-MEM and F12 medium, added with 10% heat inactivated FBS, antibiotics (100 IU/ml penicillin and 100 mg/ml streptomycin), and 2.5 $\mu\text{g}/\text{ml}$ antimycotic (Diflucan). The P(VDF-TrFE)/LiNbO₃ fiber ribbons (size $1 \times 1\text{ cm}^2$) were placed inside 6-well plates and sterilized in absolute ethanol overnight, followed by washings in sterile saline with $3\times$

antibiotics/antimycotic. Therefore, 100 000 cells were seeded onto the fiber meshes, previously coated with a 2% (w/v) sterile aqueous solution of gelatin. At the endpoint, cell viability was investigated with alamarBlue assay. Subsequently, the samples were fixed in formalin and stained with DAPI for fluorescence microscopy observation (Eclipse TI, Nikon) equipped for fluorescence analysis and an FITC filter. Samples were imaged at $5\times$ and $10\times$ magnifications, taking representative pictures for each sample.

The metabolic activity of the cells grown on the scaffolds was measured using an alamarBlue test. Data were acquired according to the manufacturer's instructions and expressed as the percentage of reduced alamarBlue (%AB_{red}). Briefly, samples ($n = 3$) and negative controls ($n = 3$) were incubated for 3 h at 37°C with the alamarBlue dye diluted in culture media. At the endpoint, 100 μl of supernatant from the sample or control was loaded into 96-well plates. The absorbance (λ) of supernatants was measured with a spectrophotometer (Victor 3; PerkinElmer, Waltham, MA, USA) under double-wavelength reading (570 and 600 nm). Finally, %AB_{red} was calculated by correlating the absorbance values and the molar extinction coefficients of the dye at selected wavelengths, following the protocol provided by the manufacturer. At the endpoint, the cell/scaffold constructs were washed twice with $1 \times$ PBS and then fixed in 1% (w/v) neutral buffered formalin for 10 min at 4°C . Samples were then counterstained with 10 $\mu\text{g}/\text{ml}$ DAPI in $1 \times$ PBS for 10 min at RT to detect cell nuclei (fluorescent in blue) and washed in $1 \times$ PBS. The specimens were observed by an inverted fluorescence microscope equipped with a digital camera (Nikon Eclipse Ti).

8. Statistical analysis

For biological studies with LiNbO₃ nanoparticles, significant differences among groups were assessed through two-way ANOVA with Tukey's HSD for unequal values by using GraphPad Prism 6.0. Data were expressed as means \pm standard deviation of three independent experiments. Statistical analysis on fiber diameter measurements was performed to assess the significant level of different processing parameters used for electrospun fiber fabrication. All data were analyzed using a one-way analysis of variance and *post hoc* test (Duncan) for multiple comparisons. Probability (p) values <0.05 were considered as statistically significant. For biological studies with P(VDF-TrFE)/LiNbO₃ fibers, significant differences among groups were assessed through t-test followed by Bonferroni correction.

III. RESULTS AND DISCUSSION

A. LiNbO₃ nanoparticles

The LiNbO₃ powder was morphologically characterized via SEM, showing submicrometric aggregates of nanoparticles [Fig. 2(a)]. An aqueous dispersion of nanoparticles was obtained for DLS analysis. Particle size and size distribution are reported in Fig. 2(b). The average size and polydispersity index (PDI) of LiNbO₃ particles were 392.25 nm and 0.517, respectively. Element analysis demonstrated the presence of Niobium (45.47 w%) of the particles [Fig. 2(c)]. XRD was used to evaluate the presence of piezoelectric crystallographic β phase in the LiNbO₃ powder. Results showed the two peaks at $2\theta = 55.97^\circ$ and 56.87° proper of the LiNbO₃ β -phase [Fig. 2(d)].

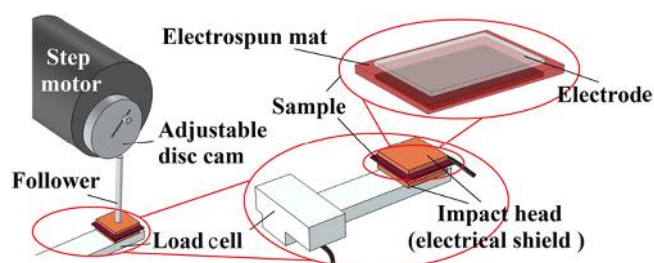


FIG. 1. Schematic view of the PiezoTester used in this study. The full explanation of this device is described in Ref. 27.

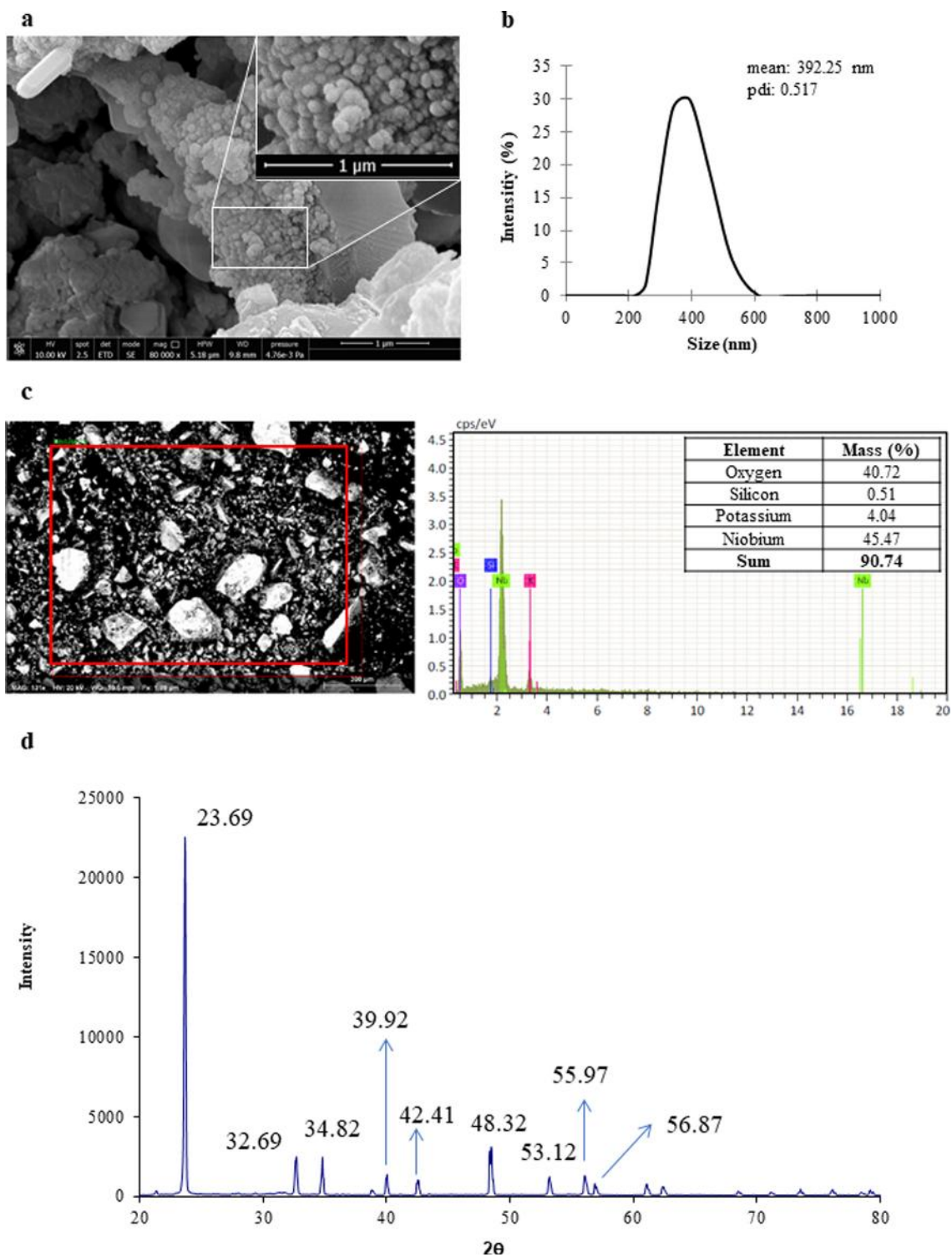


FIG. 2. Lithium niobate nanoparticle characterization: (a) SEM images of dry powder showing submicrometric clusters of nanoparticles, (b) size analysis of LiNbO_3 powder dispersion via DLS, (c) element analysis via SEM of LiNbO_3 powder, and (d) XRD analysis of LiNbO_3 powder.

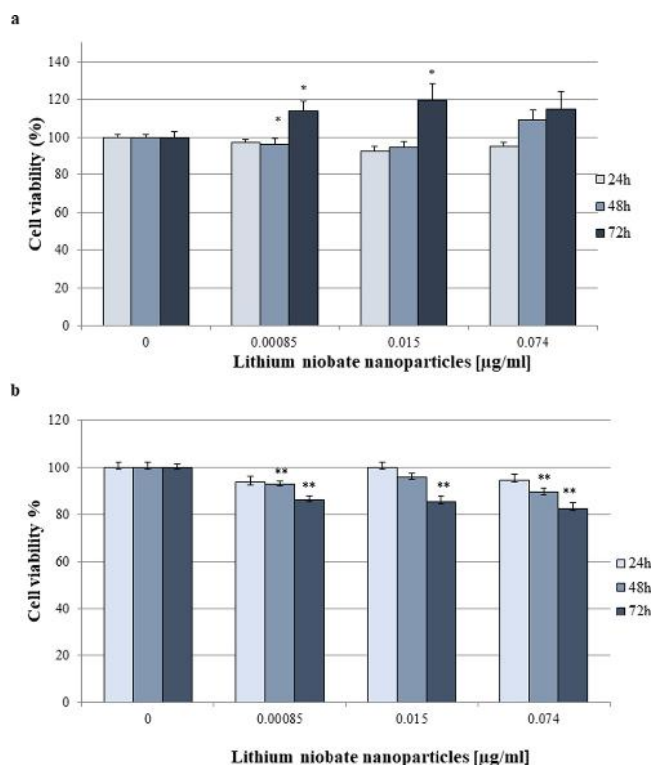


FIG. 3. Viability analysis on (a) OC-k3 cells and (b) PC12 cells treated with different concentrations of lithium niobate nanoparticles, using MTS assay, performed at 24, 48, and 72 h. Comparisons between samples were analyzed by multifactor ANOVA (Tukey's HSD for unequal values). * $p < 0.05$ between each sample and the respective control.

B. In vitro otocompatibility of LiNbO₃ nanoparticles

Figure 3(a) shows the outcomes of MTS assay performed on OC-k3 cells treated with different concentrations of LiNbO₃ nanoparticles suspended in gelatin water solution (as reported in Methods, Sec. I) at 24, 48, and 72 h. On OC-k3, LiNbO₃ induced a significant increase in cell viability after 72 h of incubation at the concentrations of 0.0085 and 0.015 µg/ml. On the other hand, on a PC12 cell line, all the concentrations tested of LiNbO₃ slightly but significantly reduced cell metabolic activity starting from 48 h exposure [Fig. 3(b)].

A morphological analysis was also performed on both cell lines treated with LiNbO₃ nanoparticle suspensions. Figures 4 and 5 show color combined morphologic analysis on OC-k3 and PC12 cells, respectively, which were treated with different concentrations of LiNbO₃, using Phalloidin Tric and DAPI fluorescent staining. OC-k3 and PC12 cells reported a good state of cellular health, evidenced by roundish nuclei (in blue) without thickening of chromatin and good cytoskeleton conformation (in red) at all doses and times tested. PC12 also revealed cell body with differentiated dendrites. The obtained results highlighted that LiNbO₃ nanoparticles at all timepoints and doses tested did not induce cell morphology alterations on both cell lines; indeed, the cell membranes and the

cytoskeletons were intact and well distended. In a similar fashion, the shape and the volume of the nuclei were normal without signs of pyknosis. Overall, LiNbO₃ nanoparticles resulted fully cytocompatible on the OC-k3 cell line. However, a reduced metabolic activity without cell morphology was observed in PC12 cells. Further experiments are needed to better clarify this behavior.

C. Immunomodulatory activity of LiNbO₃ nanoparticles

Figure 6 shows cytokine expression by HaCaT cells at 6 and 24 h obtained by RT-PCR. The results evidenced that LiNbO₃ nanoparticles induced a high immunomodulatory activity against IL-1 α , TNF- α , IL-8, and especially IL-6, intended as the ability of changing cytokine expression levels with time. They also enhanced the expression of IL-1 α and TNF- α at 24 h.

D. Antibacterial activity of LiNbO₃ nanoparticles

Lithium niobate nanoparticles also stimulated a significant increase in the production of HBD-2, which indicates the presence of an indirect antibacterial activity [Fig. 7(a)]. Figure 7(b) shows direct antimicrobial activity of LiNbO₃ nanoparticles. The presence of an antibacterial activity is revealed by the presence of a transparent halo around the disk due to the inhibition of bacterial growth (Table II). At the concentrations tested, LiNbO₃ nanoparticles were active only on *P. aeruginosa* (data not shown for *S. aureus*, since no antimicrobial activity was detected).

E. P(VDF-TrFE)/LiNbO₃ composite fibers

SEM images of pure P(VDF-TrFE) fibers and P(VDF-TrFE)/LiNbO₃ composite fibers produced at different collector velocities are shown in Fig. 8. Continuous ultrafine fibers with surface porosity were obtained in all production conditions. Increasing collector velocity improved fiber alignments in pure and P(VDF-TrFE)/LiNbO₃ composite fibers. By increasing the nanoceramic content, smaller diameter fibers were more frequently detected. LiNbO₃ particles resulted quite uniformly distributed inside the P(VDF-TrFE) fiber matrix, although, in some regions, nanoparticle aggregates were observed inducing the formation of fiber with nonuniform diameter especially at lower collector velocity (500 rpm). Element analysis and backscattered electron images also confirmed the presence of particles inside the fibers (Fig. 9).

The diameter of pure and composite fibers produced at different collector velocities is reported in the bar graph (Fig. 10). As expected, increasing collector velocity reduced the fiber diameter in both pure and composite fibers. The presence of 10% (w/w)

TABLE II. Inhibition halo measurements using *P. aeruginosa* and different concentrations of nanoparticles.

LiNbO ₃ concentration (µg/ml)	Inhibition halo (cm)
25	1.0
50	1.0
100	1.0
1000	1.2

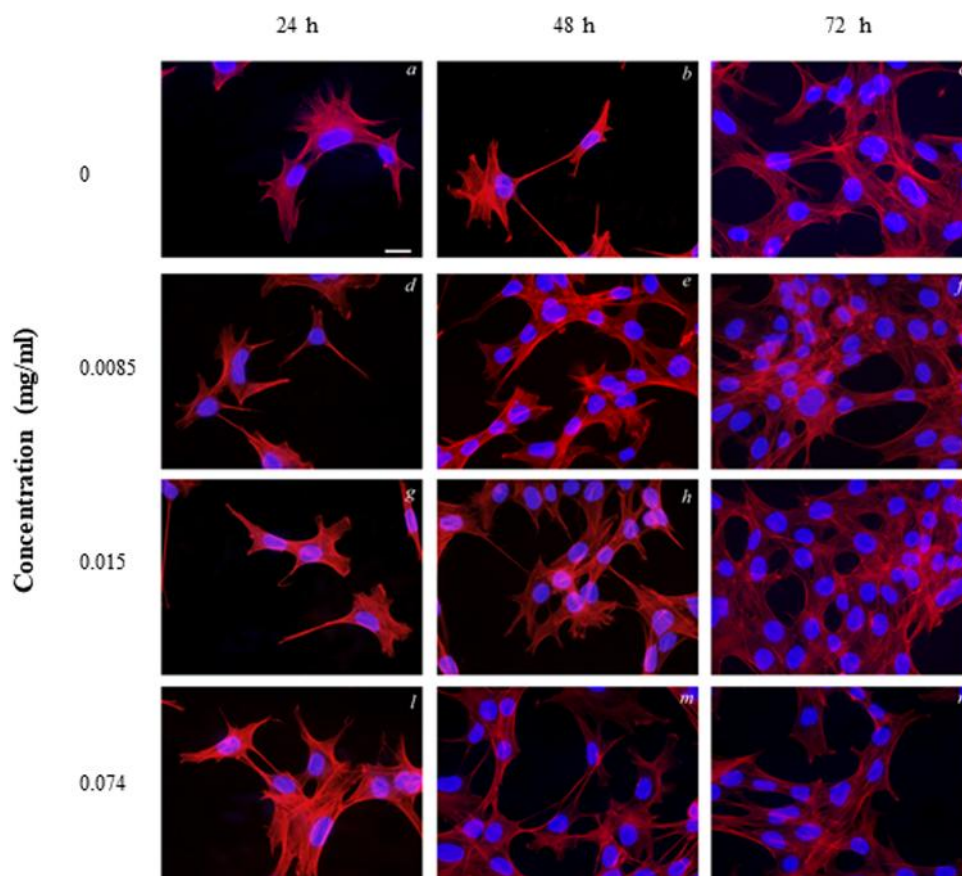


FIG. 4. Color combine morphology analysis on OC-k3 cells treated with different concentrations of lithium niobate, using Phalloidin Tric and DAPI fluorescent staining, for cytoskeleton (in red) and nuclei (in blue), respectively, at 24, 48, and 72 h. Original magnification 400 \times .

LiNbO₃ nanoparticles had no significant effect on fiber diameter of randomly oriented fibers while 20% (w/w%) LiNbO₃ nanoparticles increased fiber diameter from 1.83 ± 0.48 to $2.04 \pm 0.57 \mu\text{m}$. In the case of aligned fibers, the presence of 10% (w/w%) nanoparticles reduced fiber diameter from 1.27 ± 0.24 to $0.98 \pm 0.26 \mu\text{m}$, while the presence of 20% (w/w%) particles significantly increased fiber diameter ($1.34 \pm 0.25 \mu\text{m}$).

The stress-strain curves of pure and P(VDF-TrFE)/LiNbO₃ composite fiber are presented in Fig. 11(a). Results showed that by adding 10% (w/w%) nanoparticles, the tensile modulus of aligned pure fiber meshes reduced from 113.82 MPa down to 46.89 MPa, and elongation at break changed from 265% to 208%. Furthermore, tensile strength decreased from 21.87 to 6.67 MPa. Increasing the percentage of nanoparticles in the composite up to 20% (w/w%) decreased copolymer crystallinity (Table III); however, the tensile strength of the 80/20 (w/w%) composite fiber mesh was improved with respect to the 90/10 (w/w%) counterpart, thus suggesting a possible reinforcement action of this filler. In general, the results showed that the presence of inorganic nanoparticle inside the fibers decreased the stretchability and elongation at break of meshes.

Further investigation of the mechanical behavior was performed by DMA at RT in the constant static stress and 1% dynamic strain and frequency range of 5–100 Hz [Figs. 11(b)–11(d)]. Under these working conditions, aligned electrospun fiber meshes exhibited higher storage modulus compared to randomly oriented fibers. Results highlighted the significance of the degree of alignment and the role of straightened fibers on the mechanical properties of both pure and composite meshes. The results also confirmed that in all ranges of frequency, the composite fibers with 20% (w/w%) nanoparticles have the highest elastic modulus in comparison to other samples.

FTIR spectra of pure and P(VDF-TrFE)/LiNbO₃ composite fibers produced at different collector velocities are reported in Fig. 12. Increasing collector velocity led to an enhancement in the intensity of the crystalline bands representing β -phase at (846, 884, 1124, 1181, 1285, and 1431 cm^{-1}) [Figs. 12(a) and 12(b)]^{28,29} in both pure and composite scaffolds, but the effect of collector velocity was more pronounced in the pure ones. The presence of LiNbO₃ particles inside the fibers led to reduction in the intensities of the crystalline bands representing the β -phase in aligned fiber

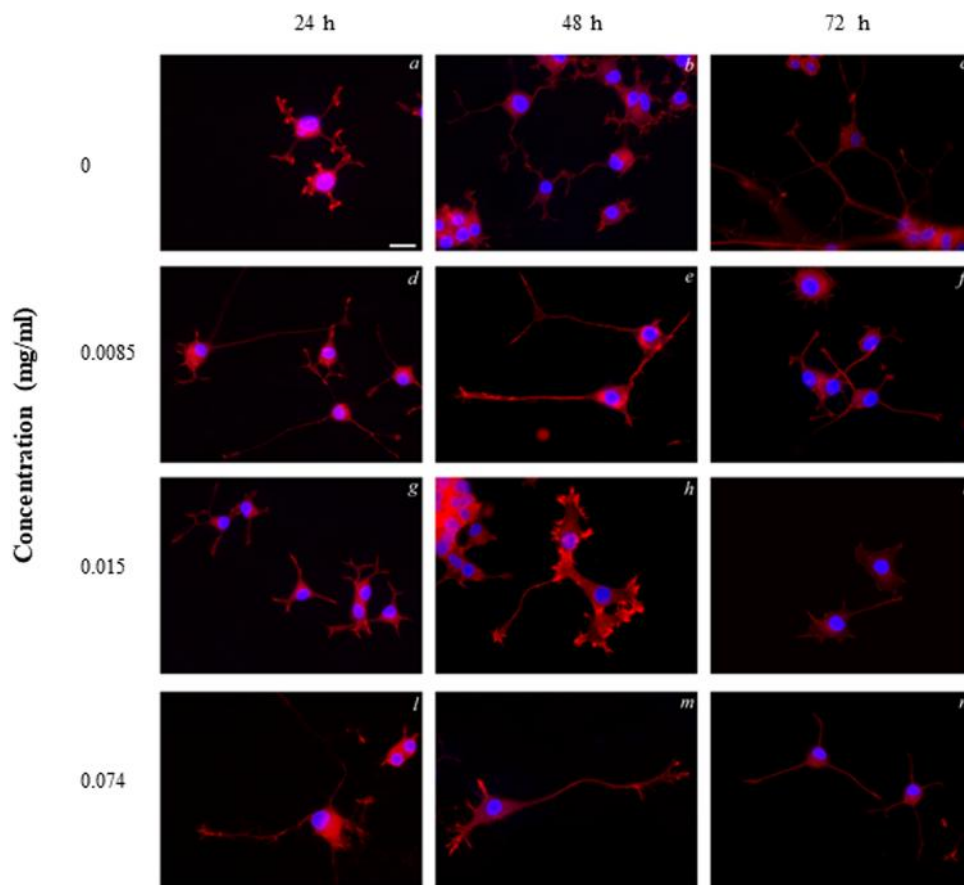


FIG. 5. Color combine morphology analysis on PC12 cells treated with different concentrations of lithium niobate, using Phalloidin Tric and DAPI fluorescent staining, for cytoskeleton (in red) and nuclei (in blue), respectively, at 24, 48, and 72 h. Original magnification 400 \times .

meshes [Fig. 12(d)], while it has no significant effect on random fiber meshes [Fig. 12(c)].

Piezoelectric properties of pure and composite electrospun fiber meshes produced at collector velocities of 500 and 4000 rpm were evaluated by a self-designed piezotester (Fig. 1). The measured output voltages and sensitivity are reported in Table IV. Increasing collector velocity up to 4000 rpm improved the output voltage of pure and composite scaffolds.

F. Cytocompatibility of PVDF-TrFE/LiNbO₃ composite fibers

The produced aligned polymer fibers (0%–20% w/w% lithium niobate) were used as scaffolds for human neuroblastoma cells SHSY-5Y as a human neural cell model. The objective of this approach concerns the implantation of such fibers and, by generating local electric charges upon BM vibration, make them behave as a scaffold to recruit and connect to neurites of the spiral ganglion nerve. Cells adhering the fibers were detected through the presence of nuclei stained with DAPI [Figs. 13(a)–13(c)]. It was noticed that

the metabolic activity of SHSY-5Y cells increased by increasing the amount of lithium niobate nanoceramics in the fibers [Fig. 13(d)].

G. Discussion

SNHL is a pathology in which hair cells, composing the sensory epithelium of the cochlea located in the organ of Corti, are damaged and do not properly transduce the acoustic signal, from mechanic (i.e., fluid waves) into electric (i.e., depolarization of spiral ganglion neurons), while the nerve can still be functioning.⁸ Many causes can bring to SNHL: exposure to noise and ototoxic drugs can reduce our hearing by damaging the sensory cells, whereas most disabling conditions include infections or genetic alterations affecting the sensory cells.³ Piezoelectric materials act as mechano-electrical transducers, since they are able to generate electric charges under mechanical force and mimic the function of the cochlear sensory epithelium.¹⁴ However, attaining a sufficient sensitivity for this specific application is still challenging.^{12,13} Piezoelectric ceramics possess higher piezoelectric properties than polymers but, for their rigid structure, they have faced

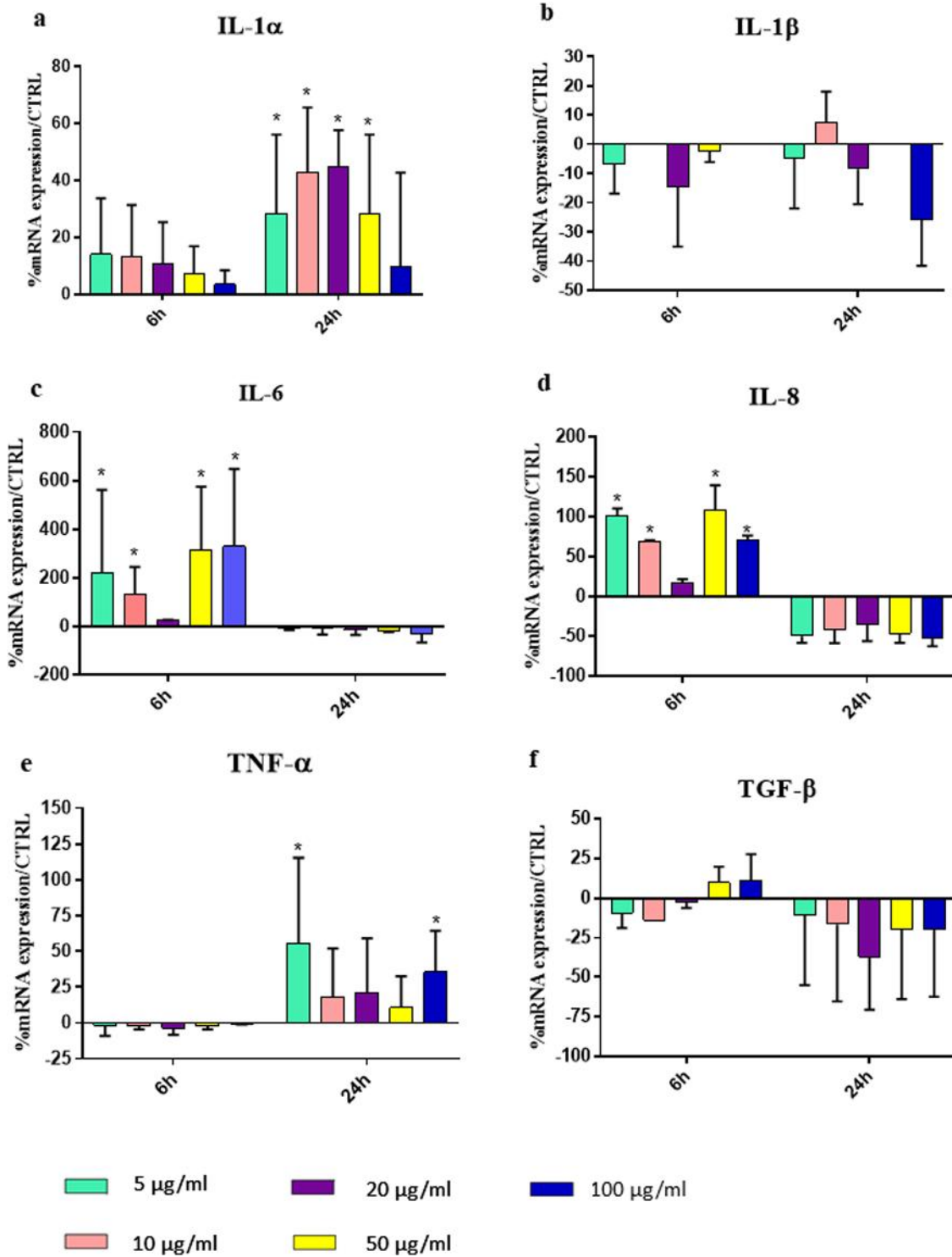


FIG. 6. Cytokine expression by HaCaT cells at 6 and 24 h obtained by RT-PCR: (a)–(e) proinflammatory cytokines; (f) anti-inflammatory cytokine. Comparisons between samples were analyzed by multifactor ANOVA (Tukey's HSD for unequal values). * $p < 0.05$ between each sample and the respective control.

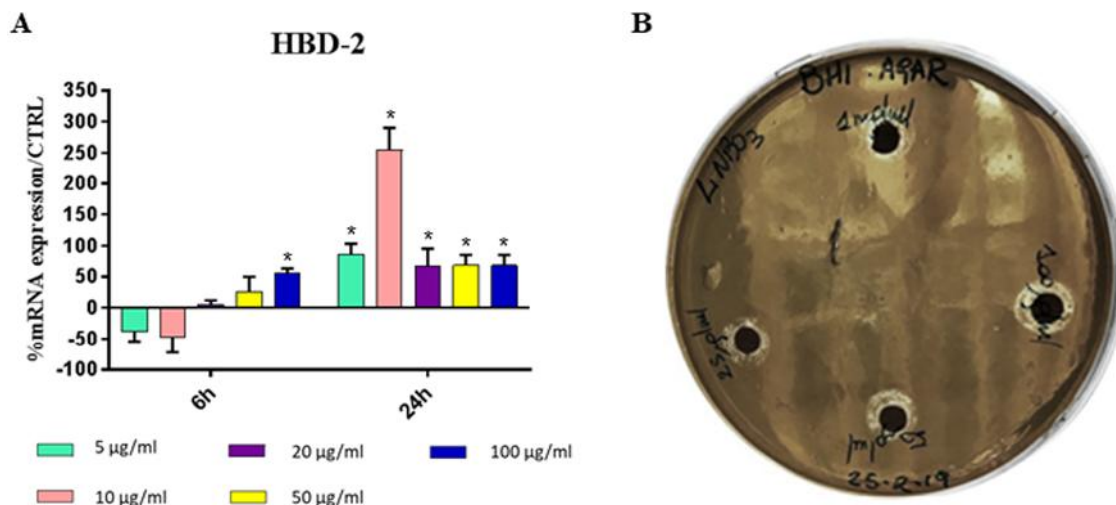


FIG. 7. Antimicrobial properties of LiNbO₃ nanoparticles: (a) indirect antimicrobial activity by HaCaT cell expression of HBD-2 gene. Comparisons between samples were analyzed by multifactor ANOVA (Tukey's HSD for unequal values). **p* < 0.05 between each sample and the respective control; (b) direct antimicrobial activity on *P. aeruginosa*.

processability problems that limit their practical applications.⁹ To overcome these limitations, in previous works, we investigated barium titanate (BaTiO₃) nanoparticles to be incorporated into PVDF fibers.⁸ In this study, we focused on lithium niobate, a lead-free ceramic entitled with excellent piezoelectric properties. Little is known on the biological effects of this ceramic material. Therefore, we performed an extensive biological investigation to disclose ototoxic effects, in particular, by using an *in vitro* model of the inner ear organ.³⁰ Moreover, we investigated the immunomodulatory effects as well as potential direct and indirect antibacterial properties using ear contaminating pathogens, such as *S. aureus* and *P. aeruginosa*. Finally, we designed a processable structure using P(VDF-TrFE)/LiNbO₃ composite fibers with attractive features for human neural cells, which was fully characterized and showed improved sensitivity for cochlear stimulation.

As obtained, pristine LiNbO₃ particulate was in the form of aggregated nanoparticles that could be disaggregated within 200–600 nm size range via sonication prior to be administered to different cell lines. The first set of experiments aimed at highlighting the LiNbO₃ nanoparticle interaction with a model of cochlear cells, including inner ear epithelial cells OC-k3 and neural-like cells PC12. Our results pointed out a very good compatibility of these nanoparticles *in vitro*, in particular with OC-k3 cells, which are representative of the delicate cochlear epithelium.³⁰ In a future device integrated with the cochlear organ, preserving any residual hearing capacity after implantation is of utmost importance. Differently, PC12 cells experienced a decrease in metabolic activity, while preserving healthy and differentiated morphology at the tested concentrations. Further experiments are needed to elucidate this behavior, which for other piezoelectric nanoceramics, such as BNNTs, was reported at higher doses.³¹ The obtained morphological results clearly showed differentiating PC12 cells at all the times and nanoparticle concentrations tested, which could suggest a

differentiative stimulus provided by these nanoparticles. In addition to otocompatibility, lithium niobate nanoparticles demonstrated functional properties toward HaCaT cells, which were used as an additional (nonsensory) human epithelial source to characterize the innate immune reactions of this nanoparticles toward human epithelial cells,³² being OC-k3 and PC12 of animal origin. Our findings demonstrated that LiNbO₃ nanoparticles induced a marked immunoregulatory response on these cells by modulating the expression of proinflammatory cytokines IL-1α, TNF-α, IL-8, and, in particular, IL-6 after 24 h exposure. Specifically, IL-6 and IL-8 were downregulated with time, whereas IL-1α and TNF-α were upregulated. All these cytokines are involved in the wound healing process, which takes place after implant surgery. IL-6 functions as an autocrine, paracrine, and endocrine mediator of inflammation by acting as a growth factor for immune cells.³³ IL-8 is secreted by several cell types, including monocytes-macrophages, fibroblasts, endothelial cells, and keratinocytes. The most important function of IL-8 is the attraction and activation of polymorphonuclear leukocytes, but it also plays a role in angiogenesis.³⁴ Inflammation is characterized by an interplay between pro- and anti-inflammatory cytokines. Proinflammatory cytokines are involved in the upregulation of host immune response by promoting systemic inflammation; on the other hand, the anti-inflammatory cytokines modulate the intensity of the inflammatory process, thus contributing to its resolution. The LiNbO₃ ability of modulating the expression of IL-6 and IL-8 could play a beneficial role *in vivo*, by reducing the extent or duration of a postimplant inflammatory response. Instead, the increase of IL-1α and TNF-α usually promotes local inflammation,³⁵ being TNF-α also involved in reducing infection risk via platelet adhesiveness activation.³⁶

In HaCaT cells, lithium niobate nanoparticles were able to upregulate the expression of an antimicrobial peptide, HBD-2, which acts as an endogenous antibiotic against Gram-positive and

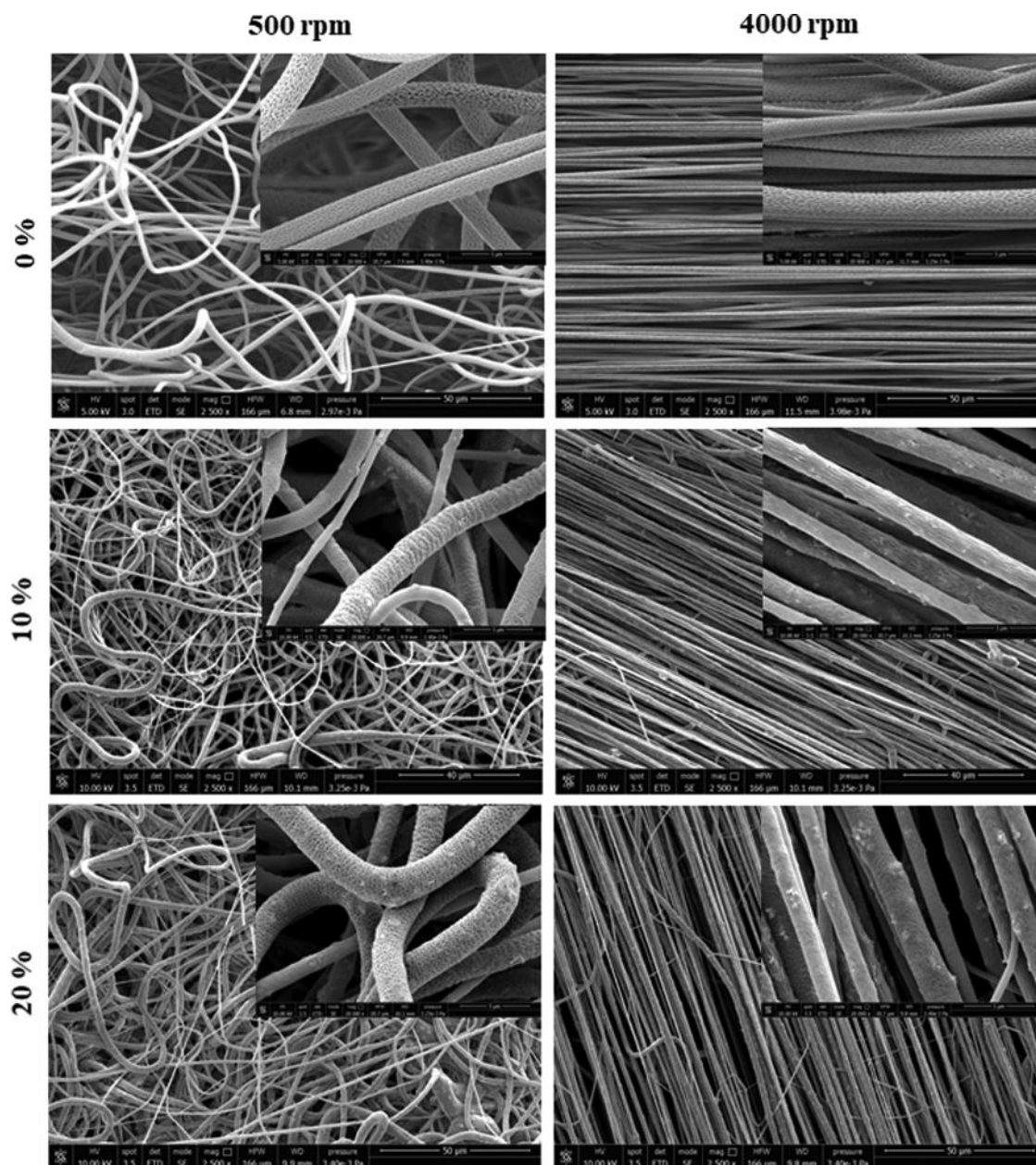


FIG. 8. Morphology of P(VDF-TrFE)/LiNbO₃ composite fibrous meshes at different lithium niobate weight concentrations and electrospun at different collector velocities as obtained via SEM: (a) 0% (pure polymer) at (a1) 500 rpm (isotropic) and (a2) 4000 rpm (anisotropic); (b) 10% (w/w%) at (b1) 500 rpm (isotropic) and (b2) 4000 rpm (anisotropic); and (c) 20% (w/w%) at (c1) 500 rpm (isotropic) and (c2) 4000 rpm (anisotropic).

Gram-negative bacteria, fungi, and the envelope of some viruses, as a part of the innate immune response.³⁷ In addition, these nanoparticles showed a direct antibacterial activity against *P. aeruginosa*, which is commonly found in *otitis chronica*, and is often resistant to most commonly used antibiotics.³⁸ Overall, we showed that LiNbO₃ nanoparticles possess beneficial properties and promote

proficient interactions with the biological matter, which could be exploited as an interface material to produce implanted devices, including, but not limited to next generation CIs.³⁹ A different emerging approach is the development of fully implantable microphones.⁴⁰ Park *et al.* presented a concept for an innovative implantable device to detect travelling pressure waves from a fluid-filled

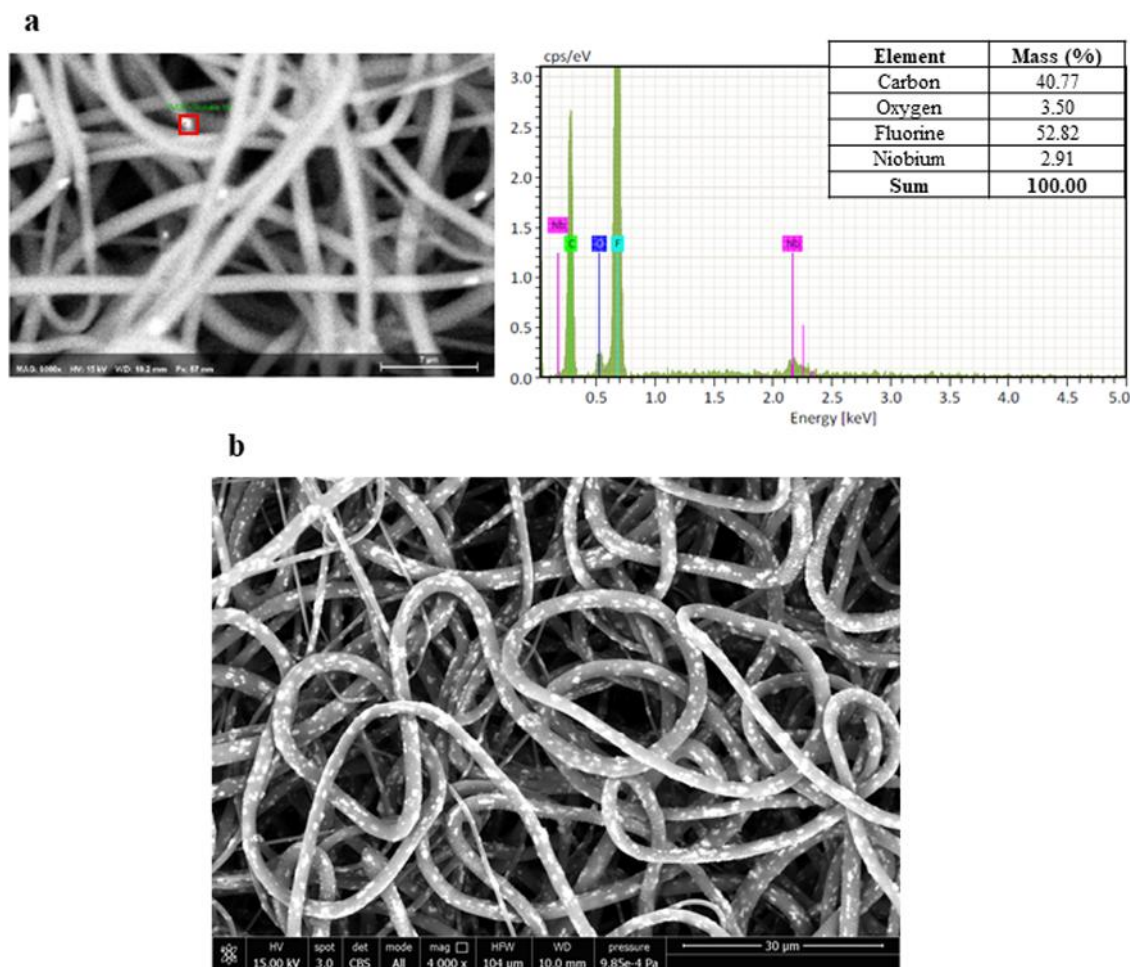


FIG. 9. (a) Element analysis and (b) backscattered electron images of P(VDF-TrFE)/LiNbO₃ composite fibrous meshes.

cochlea. The proposed solution encompassed a passive PVDF-based film microphone positioned at the round window level. However, despite the encouraging results on gerbil and guinea pigs *in vivo* models, the authors believed that the design of such a system requires further improvement iterations to increase its sensitivity. To show the potentiality of their system, indeed, they maximized its performance by increasing the dimensions of the microphone to the detriment of surgical needs.⁴⁰ Having better sensitive piezoelectric materials would allow this system to be miniaturized. After implantation of any permanent devices in the human body, inflammatory reactions take place, which ultimately support fibrous scar formation and possible infections by bacterial colonization easily occurring in the interface region between the implant and the avascular fibrotic capsule. Consequently, the thicker the capsule, the lower effectiveness of a signal transmission. To deal with low sensitivity, which is the case of PVDF-based devices and their composites, any interfacial resistances should be minimized or avoided. Ideally, having immunomodulatory and

antibacterial materials would possibly allow a normal healing with reduced fibrosis and improved device performance. In order to further enhance the contact between resident neurites and the piezoelectric functional materials, we designed the piezo-active substrate under an *in vivo* tissue engineering approach.⁸

Ultrafine fibers as obtained via electrospinning have been reported to promote neural cell activity via promoting cell/interface contact,⁴¹ and polymer/ceramic composite fibers are able to improve the piezoelectric coefficients of transducers.⁴² P(VDF-TrFE)/LiNbO₃ fibers were produced by electrospinning with LiNbO₃ weight ratios in the range of 0%–20%. The production of random-to-aligned electrospun fibers was also performed by changing the rotating collector velocity. The morphology of the obtained meshes was characterized and the dispersion of LiNbO₃ nanoparticles inside the P(VDF-TrFE) fibers was analyzed.

Continuous ultrafine fibers were formed. Increasing collector velocity reduced fiber diameter, which could be attributed to the higher tension of the rotating collector⁴³ and also improved the

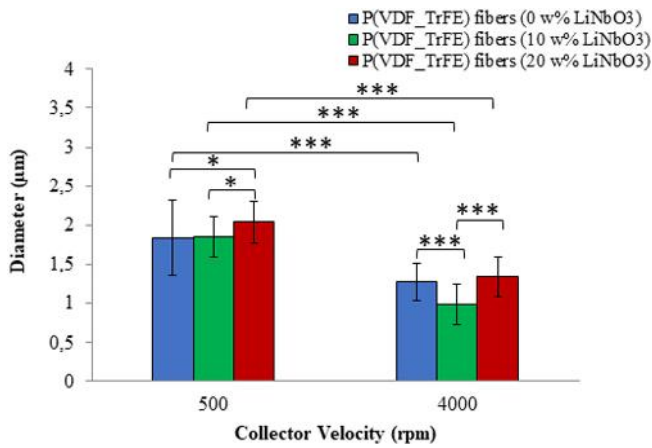


FIG. 10. Bar graph showing diameters of P(VDF-TrFE)/LiNbO₃ composite fibers obtained at different lithium niobate weight concentrations and electrospun at different collector velocities.

fiber alignment in both pure and composite P(VDF-TrFE)/LiNbO₃ fiber meshes. The particular micro-/nanofibrous architecture and topography of electrospun scaffolds are very important, since they act as a microenvironment at the cellular level, which can enable certain cell interaction through functional and morphological responses.^{41,44} Electrospun scaffolds can have random up to aligned fibers. The importance of fiber alignment in neural tissue engineering was confirmed by different studies and anisotropic properties of aligned fibers were best suitable to provide spatial guidance for neurite outgrowth.^{43,44} LiNbO₃ particles were quite uniformly distributed inside the P(VDF-TrFE) fiber matrix although, in some regions, nanoparticle aggregation was observed, with the formation of fibers with nonuniform diameter, especially at low collector velocity (i.e., 500 rpm). Phase separation and evaporative cooling mechanisms accrued in high RH (i.e., 46%) led to the formation of fibers with surface nanoporosity.⁴⁵ Since P(VDF-TrFE) is hydrophobic, at high RH, the surface of fibers will be wetted and water molecules will grow into water droplets, leaving nanosized indentations on the fiber surface upon evaporation. The presence of LiNbO₃ nanoparticles inside the fibers improved water permeability and led to the formation of composite fibers with lower surface porosity.⁴⁶ Since the cochlea is filled with aqueous solutions that allow signal transduction by transmitting mechanical vibrations to the BM, hydrophilicity is considered an important property for designing a material integrating with the cochlear tissues and acting as a good tissue-liquid interface.

The mechanical properties of fiber meshes rely on the arrangement of the fibers in a layer and on the mechanical properties of the single fibers. Increasing the rotative velocity of the collector to 4000 rpm induced the copolymer chain orientation followed by the straight improvement of the fibers. On the other hand, as shown in SEM analysis, the high alignment of ultrafine fibers produced at 4000 rpm led to increased number of fibers to be involved in the cross-sectional area during stretching. Therefore, the applied

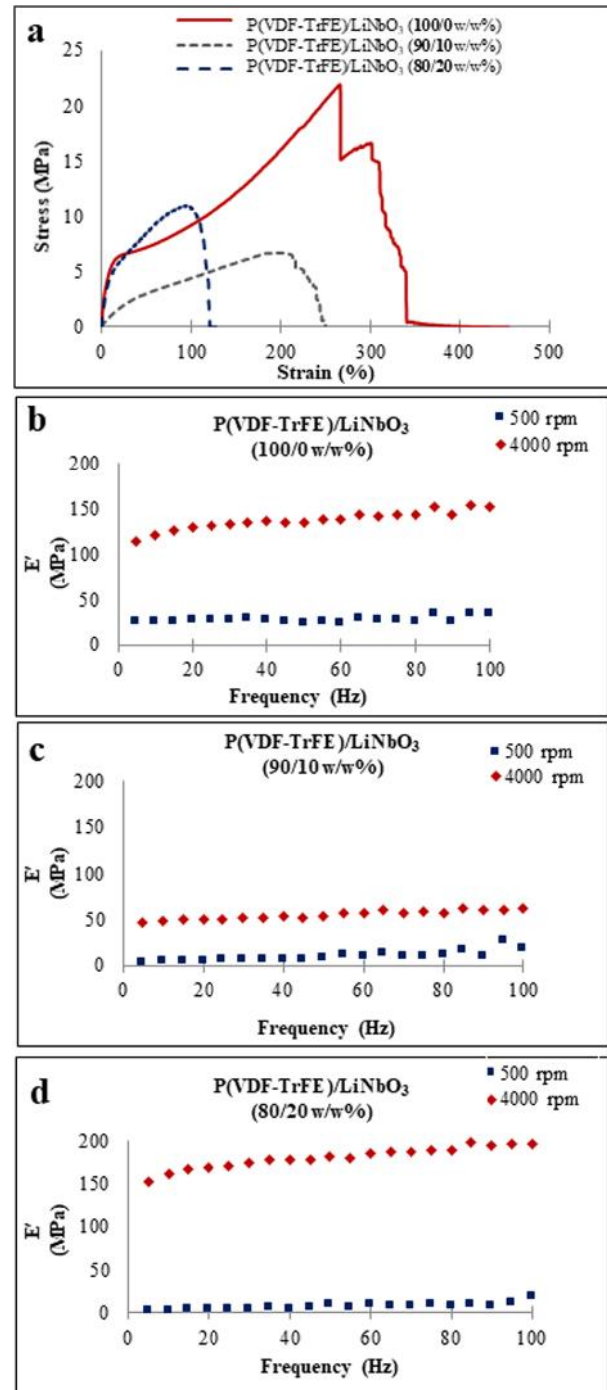


FIG. 11. Mechanical properties of P(VDF-TrFE)/LiNbO₃ composite fibers obtained at different LiNbO₃ weight concentrations and electrospun at different collector velocities: (a) Tension-mode tests of fibers collected at 4000 rpm with different compositions and (b)–(d) DMA analysis. (b) Pure P(VDF-TrFE) fibers, (c) P(VDF-TrFE)/LiNbO₃ composite (10% w/w%), and (d) P(VDF-TrFE)/LiNbO₃ composite (20% w/w%) fibers.

TABLE III. Thermal properties of pure and P(VDF-TrFE)/LiNbO₃ fibers produced at 4000 rpm.

P(VDF-TrFE)/ LiNbO ₃ (w/w%)	T _m (°C)	Melting enthalpy (J/g)	Crystallinity (%)
100/0	152.19	29.43	32.18
90/10	146.90	30.62	30.13
80/20	147.25	33.23	29.06

force is supported by high numbers of fibers, which resulted in enhanced tensile strength.^{47,48}

Due to parallel fiber/stress directions, a higher force is required to create the same strain in aligned fibers than random ones. Therefore, aligned fiber meshes usually show a superior elastic modulus in comparison to their random counterparts. However, LiNbO₃ nanoparticles can act as stress concentrators,

initiate cracking, and eventually decrease mechanical properties. The presence of nanoparticles inside the fibers can reduce the density of intermolecular forces in the polymer matrix and led to a decrement in mechanical properties.⁴⁹ Therefore, it is important to consider the mechanical effect of the filler in relation to shape, size, and concentration. In our study, the lithium niobate nanoparticles at 10% w/w% reduced the mechanical properties of the fibers, whereas this effect was ameliorated at 20% w/w% concentration. In piezoelectric CIs, the material is going to work in the elastic region, under nanometric displacements, with a reduced viscoelastic behavior, which complies with all the obtained composite fiber meshes.

FTIR and DSC were used to evaluate the presence of piezoelectric crystallographic β-phase in the produced scaffolds, which is related to the piezoelectric properties of the polymer. Also here, an increase in the rotating collector velocity caused an increase in the crystalline structure and output voltage.^{27,50} The presence of 20% (w/w%) LiNbO₃ nanoparticles inside the aligned fiber meshes

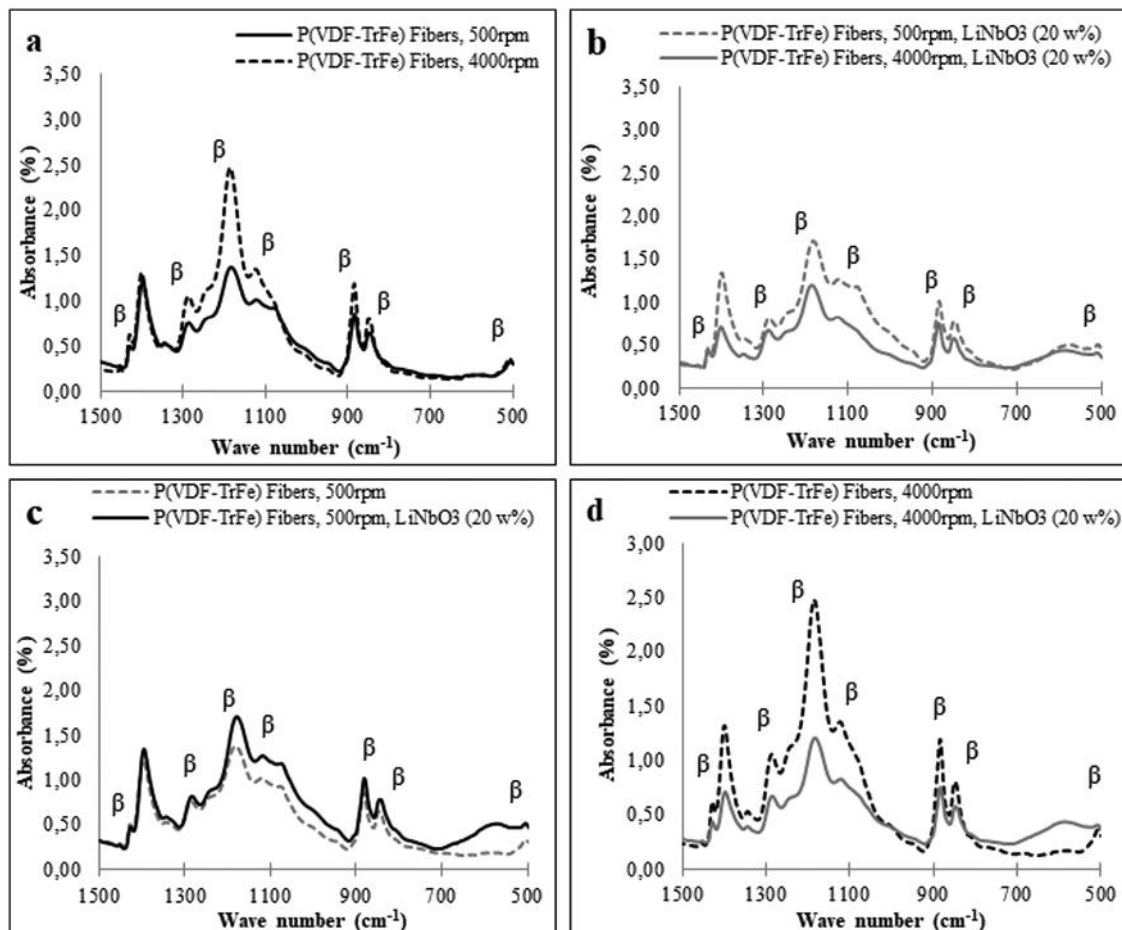


FIG. 12. Polarized light FTIR analysis of P(VDF-TrFE)/LiNbO₃ composite fibers obtained at different lithium niobate weight concentrations and electrospun at different collector velocities.

TABLE IV. Piezoelectric properties of pure and LiNbO₃/P(VDF-TrFE) composite fibers obtained at different lithium niobate weight concentrations and electrospun at different collector velocities. All tests were performed under a 2.12 N applied load.

Collector velocity (rpm)	LiNbO ₃ /P(VDF-TrFE) (w/w %)	V _{out} (mV)	Sensitivity (mV/N)	Thickness (μm)	Normalized sensitivity (mV/N μm)
500	100/0	45 ± 5	21.20	40	0.53
500	90/10	50 ± 4	23.58	60	0.39
500	80/20	40 ± 4	18.86	50	0.37
4000	100/0	80 ± 1	37.73	40	0.94
4000	90/10	60 ± 3	28.30	40	0.70
4000	80/20	90 ± 2	42.45	40	1.06

significantly increased the fraction of β-phase and subsequently its output voltage while had no considerable effect on the fraction of β-phase in randomly oriented fibers mesh. In aligned fibers, the output voltage doubled by doping the copolymer with 20% (w/w%) LiNbO₃. This finding is in agreement with a previous study using BaTiO₃ nanoparticles.⁸

Finally, the produced ceramic/polymer fiber meshes in the range of 0%–20% (w/w%) LiNbO₃ were used as scaffolds for human neuroblastoma cells SHSY-5Y, as a neural cell model, in static conditions, revealing the presence of cells adhered on the fibers and a metabolic activity enhancement effect by increasing lithium niobate concentration. Strategies for functional nanoparticle incorporation

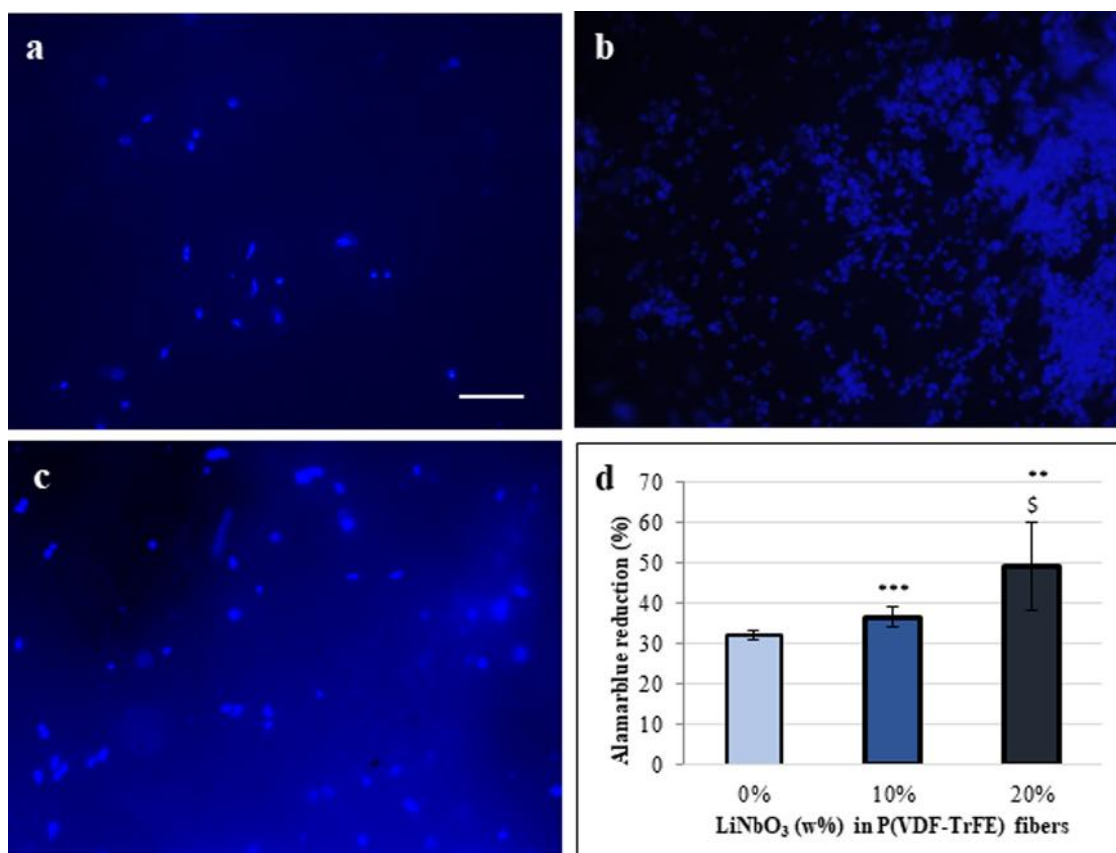


FIG. 13. SHSY-5Y cells grown for 7 days onto aligned P(VDF-TrFE)/LiNbO₃ composite fibers at different LiNbO₃ concentrations: (a)–(c) DAPI staining of (a) 0% (pure polymer), (b) 10%, and (c) 20% w/w%; (a)–(c) scale bar = 100 μm; original magnification 100×. (d) Metabolic activity results as obtained with alamarBlue assay. Statistical analysis results indicated: 0% vs 10% (**p = 0.0003), 0% vs 20% (**p = 0.0008), and 10% vs 20% (\$p = 0.004).

within electrospun fibers in the ear are, indeed, important to combine bioactive with regenerative properties.⁵¹

Having biofunctional nanostructured piezoelectric materials with improved sensitivity would move a step forward to the development of cost-effective magnetocompatible, miniaturized perpetual and wireless cochlear stimulation devices, with improved quality of life and possibly of hearing for deaf people.

IV. SUMMARY AND CONCLUSIONS

SNHL affects the cochlea and is a leading cause of deafness. Usually, the lack, death, or malfunction of sensory cells deputed to transduction of mechanic-into-electric signals generates SNHL. To date, poor regenerative capacity has been found in this organ, and the only therapeutic option clinically available relies on CIs. Piezoelectric materials can play a role in this scenario by simply mimicking the function of the cochlear sensory epithelium. In this study, we investigated lithium niobate as a potential candidate material for next generation CIs. Lithium niobate nanoparticles resulted otocompatible *in vitro* with OC-k3 cells, had a strong immunomodulatory activity, and enhanced HBD-2 in HaCaT epithelial cells, and also showed direct antibacterial activity against *P. aeruginosa*. Moreover, these nanoparticles were efficiently incorporated into P(VDF-TrFE) fibers via electrospinning. Aligned composite fibers at 20% (w/w%) lithium niobate showed an enhanced piezoelectric response, namely, 90 ± 2 mV, with respect to their random counterparts, namely, 40 ± 4 mV, under an applied load of 2.12 N. Finally, these composite fibrous structures supported human neural-like cell growth *in vitro*.

Concluding, even though more research effort is needed in this area to reach a suitable electric performance, electroactive materials combining nanotechnology and tissue engineering show promise for cochlear stimulation and otoprotection.

ACKNOWLEDGMENTS

NANOSPARKS Project (MISTI, MIT-UNIFI program 2017) and Finalized Research (Italian Ministry of Health, No. RF-2011-02350464) are gratefully acknowledged for funding this study. CISUP—Centre for Instrumentation Sharing—University of Pisa is acknowledged for SEM analysis. The authors would like to thank Delfo D'Alessandro, University of Pisa, for his technical support to biological characterization.

REFERENCES

¹W. Wu, S. Bai, M. Yuan, Y. Qin, Z. L. Wang, and T. Jing, *ACS Nano* **6**, 6231 (2012).
²R. Mittal, S. A. Pena, A. Zhu, N. Eshraghi, A. Fesharaki, E. J. Horesh, J. Mittal, and A. A. Eshraghi, *Artif. Cells Nanomed. Biotechnol.* **47**, 1312 (2019).
³F. Valente, L. Astolfi, E. Simoni, S. Danti, V. Franceschini, M. Chicca, and A. Martini, *J. Drug Delivery Sci. Technol.* **39**, 28 (2017).
⁴C. Rathnam, S.-T. D. Chueng, Y.-L. M. Ying, K.-B. Lee, and K. Y. Kwan, *Front. Cell. Neurosci.* **13**, 493 (2019).
⁵J.-H. Lee, M. Y. Lee, Y. Lim, J. Knowles, and H.-W. Kim, *J. Tissue Eng.* **9**, 2041731418808455 (2018).
⁶E. Simoni, G. Orsini, M. Chicca, S. Bettini, V. Franceschini, A. Martini, and L. Astolfi, *Cytotherapy* **19**, 909 (2017).

⁷L. Astolfi, V. Guarani, N. Marchetti, E. Olivetto, E. Simoni, A. Cavazzini, C. Jolly, and A. Martini, *J. Biomed. Mater. Res. Part B Appl. Biomater.* **102**, 267 (2014).
⁸C. Mota *et al.*, *Mater. Design* **122**, 206 (2017).
⁹B. Azimi, M. Milazzo, A. Lazzeri, S. Berrettini, M. J. Uddin, Z. Qin, M. J. Buehler, and S. Danti, *Adv. Healthcare Mater.* **9**, 1901287 (2019).
¹⁰R. Calio, U. Rongala, D. Camboni, M. Milazzo, C. Stefanini, G. de Petris, and C. Oddo, *Sensors* **14**, 4755 (2014).
¹¹S. Danti, *Boron Nitride Nanotubes in Nanomedicine* (Elsevier, Oxford, UK, 2016).
¹²N. Mukherjee and R. D. Roseman, *MRS Online Proc. Libr. Arch.* **604**, 79 (1999).
¹³N. Mukherjee, R. D. Roseman, and J. P. Willging, *Jpn. Soc. Biomater. Aust. Soc. Biomater. Korean Soc. Biomater.* **53**, 181 (2000).
¹⁴T. Inaoka, H. Shintaku, T. Nakagawa, S. Kawano, H. Ogita, T. Sakamoto, S. Hamanishi, H. Wada, and J. Ito, *Proc. Natl. Acad. Sci. U.S.A.* **108**, 18390 (2011).
¹⁵G. von Békésy, *Nature* **225**, 1207 (1970).
¹⁶R. G. Kepler and R. A. Anderson, *J. Appl. Phys.* **49**, 4490 (1978).
¹⁷F. Chen, L. Kong, W. Song, C. Jiang, S. Tian, F. Yu, L. Qin, C. Wang, and X. Zhao, *J. Materiomics* **5**, 73 (2019).
¹⁸N. C. Carville, L. Collins, M. Manzo, K. Gallo, B. I. Lukasz, K. K. McKayed, J. C. Simpson, and B. J. Rodriguez, *J. Biomed. Mater. Res. Part A* **103**, 2540 (2015).
¹⁹N. C. Carville, S. M. Neumayer, M. Manzo, K. Gallo, and B. J. Rodriguez, *ACS Biomater. Sci. Eng.* **2**, 1351 (2016).
²⁰J. Li *et al.*, *Adv. Healthcare Mater.* **4**, 998 (2015).
²¹E. Simoni, F. Valente, L. Boge, M. Eriksson, E. Gentilin, M. Candito, D. Cazzador, and L. Astolfi, *Int. J. Pharm.* **572**, 118788 (2019).
²²X. Du *et al.*, *Mol. Ther.* **26**, 1313 (2018).
²³M. Alavi and A. Nokhodchi, *Carbohydr. Polym.* **227**, 115349 (2019).
²⁴S. Danti, G. Ciofani, S. Moscato, D. D'Alessandro, E. Ciabatti, C. Nesti, R. Brescia, G. Bertoni, A. Pietrabissa, M. Lisanti, M. Petrini, V. Mattoli, and S. Berrettini, *Nanotechnology* **24**, 465102 (2013).
²⁵V. Marchesano, O. Gennari, L. Mecozzi, S. Grilli, and P. Ferraro, *ACS Appl. Mater. Interfaces* **7**, 18113 (2015).
²⁶J. Kim, J. H. Lee, H. Ryu, J.-H. Lee, U. Khan, H. Kim, S. S. Kwak, and S.-W. Kim, *Adv. Funct. Mater.* **27**, 1700702 (2017).
²⁷M. S. Sorayani Bafqi, A. H. Sadeghi, M. Latifi, and R. Bagherzadeh, "Design and fabrication of a piezoelectric out-put evaluation system for sensitivity measurements of fibrous sensors and actuators," *J. Ind. Text.* (published online).
²⁸K. Tashiro, Y. Itoh, M. Kobayashi, and H. Tadokoro, *Macromolecules* **18**, 2600 (1985).
²⁹M. A. Bachmann and J. L. Koenig, *J. Chem. Phys.* **74**, 5896 (1981).
³⁰L. Astolfi, E. Simoni, and A. Martini, *Hear. Balance Commun.* **13**, 166 (2015).
³¹G. Ciofani *et al.*, *ACS Nano* **4**, 6267 (2010).
³²S. Danti, L. Trombi, A. Fusco, B. Azimi, A. Lazzeri, P. Morganti, M.-B. Coltelli, and G. Donnarumma, *Int. J. Mol. Sci.* **20**, 2669 (2019).
³³J. Scheller, A. Chalaris, D. Schmidt-Arras, and S. Rose-John, *Biochim. Biophys. Acta Mol. Cell Res.* **1813**, 878 (2011).
³⁴A. E. Koch, P. J. Polverini, S. L. Kunkel, L. A. Harlow, L. A. DiPietro, V. M. Elnor, S. G. Elnor, and R. M. Strieter, *Science* **258**, 1798 (1992).
³⁵C. A. Dinarello, *Cytokine Growth Factor Rev.* **8**, 253 (1997).
³⁶E. Esposito and S. Cuzzocrea, *Curr. Med. Chem.* **16**, 3152 (2009).
³⁷G. Donnarumma, I. Paoletti, A. Fusco, B. Perfetto, E. Buommino, V. de Gregorio, and A. Baroni, in *Advances in Microbiology, Infectious Diseases and Public Health* (Springer, Basel, Switzerland, 2015), pp. 59–76.
³⁸T.-F. Mah, B. Pitts, B. Pellock, G. C. Walker, P. S. Stewart, and G. A. O'toole, *Nature* **426**, 306 (2003).
³⁹A. Mitchell-Innes, S. R. Saeed, and R. Irving, in *Advances in Hearing Rehabilitation* (Karger, Basel, Switzerland, 2018), pp. 105–113.
⁴⁰S. Park, X. Guan, Y. Kim, F. (Pete) X. Creighton, E. Wei, I. Kymissis, H. H. Nakajima, and E. S. Olson, *Trends Hear.* **22**, 2331216518774450 (2018).

- ⁴¹J. Xie, M. R. MacEwan, X. Li, S. E. Sakiyama-Elbert, and Y. Xia, *ACS Nano* **3**, 1151 (2009).
- ⁴²N. Mukherjee, A. Shukla, A. Dwivedi, R. D. Roseman, and D. F. Thompson, *Smart Structures and Materials 2003: Electroactive Polymer Actuators and Devices (EAPAD)* (SPIE, Bellingham, WA, 2003), pp. 309–318.
- ⁴³P. Viswanathan, M. G. Ondeck, S. Chirasatitsin, K. Ngamkham, G. C. Reilly, A. J. Engler, and G. Battaglia, *Biomaterials* **52**, 140 (2015).
- ⁴⁴Y.-S. Lee, G. Collins, and T. L. Arinzeh, *Acta Biomater.* **7**, 3877 (2011).
- ⁴⁵L. Huang, N.-N. Bui, S. S. Manickam, and J. R. McCutcheon, *J. Polym. Sci. Part B Polym. Phys.* **49**, 1734 (2011).
- ⁴⁶S. Liang, K. Xiao, Y. Mo, and X. Huang, *J. Membr. Sci.* **394**, 184 (2012).
- ⁴⁷W. E. Teo and S. Ramakrishna, *Nanotechnology* **17**, R89 (2006).
- ⁴⁸P. Kiselev and J. Rosell-Llompart, *J. Appl. Polym. Sci.* **125**, 2433 (2012).
- ⁴⁹H. Wang, Y. Li, Y. Zuo, J. Li, S. Ma, and L. Cheng, *Biomaterials* **28**, 3338 (2007).
- ⁵⁰J. Li, C. Zhao, K. Xia, X. Liu, D. Li, and J. Han, *Appl. Surf. Sci.* **463**, 626 (2019).
- ⁵¹C. Günday *et al.*, “Ciprofloxacin-loaded polymeric nanoparticles incorporated electrospun fibers for drug delivery in tissue engineering applications,” *Drug Deliv. Transl. Res.* (published online).